Design, Modeling, and Control of an Aerial Robot DRAGON: A Dual-Rotor-Embedded Multilink Robot With the Ability of Multi-Degree-of-Freedom Aerial Transformation

Moju Zhao, Tomoki Anzai, Fan Shi, Xiangyu Chen, Kei Okada, and Masayuki Inaba

***Abstract*—In this letter, we introduce a novel transformable aerial robot called DRAGON, which is a dual-rotor-embedded multilink robot with the ability of multi-degree-of-freedom (DoF) aerial transformation. The new aerial robot can control the full pose in $\mathsf{SE}(3)$ regarding the center of gravity (CoG) of multilinks and can render the multi-DoF aerial transformation, which is accomplished by the original two-DoF force vectoring mechanism on each link called the dual-rotor gimbal module. The dynamics is derived on the basis of the special definition of CoG orientation, followed by a control method decoupled into thrust force control and rotor gimbal control. In the thrust force control, the minimum force norm is considered to avoid force saturation, and the rotor gimbal control method is developed to enhance both translational and rotational stabilities during hovering and large-scale aerial transformation. The prototype composed of four links is constructed, and associated preliminary experiments are performed. The feasibility of the novel mechanical design and the proposed control method for the aerial transformation is demonstrated.**

***Index Terms*—Aerial systems: mechanics and control, motion control.**

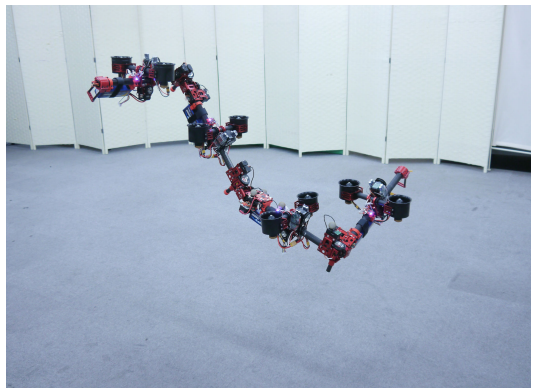

Fig. 1. Photograph of the hovering motion of DRAGON: **D**ual-rotor embedded multilink **R**obot with the **A**bility of multi-de**G**ree-of-freedom aerial transformati**ON**.

I. Introduction

MULTIROTOR aerial robots are rapidly being developed to perform various applications such as inspection [1] and surveillance [2]. Rotor disks are generally aligned in a single plane to simplify their structures, thus leading to underactuation and differential flatness [3]. Although it is a challenge for traditional multirotors to control full pose in $\mathsf{SE}(3)$, including hovering at an arbitrary attitude, some studies still achieved aggressive and agile maneuvering in $\mathsf{SE}(3)$, e.g., flying through narrow gaps (e.g., [4], [5]). For such aggressive motion, sufficient space is indispensable for run-up before passing, as well as deceleration after passing, thus implying that the environment should be well-known, particularly the one behind the gap. Otherwise, the robot might clash into unknown objects after passing through the gap. Therefore, under an unknown circumstance, the robot is required to fly slowly for simultaneous onboard reactive perception, which is not the case for the aforementioned aggressive maneuvering.

To overcome this limitation, novel designs for multirotor have been achieved recently to perform full pose in $\mathsf{SE}(3)$. For instance, different omni-directional aerial robots have been achieved with the optimized rotor configuration to maximize either the agility [6] or the control wrench [7] at an arbitrary pose. Compared with the fixed rotor configuration designs, aerial robots involving rotor tilting mechanism have been also developed (e.g., [8]–[10]) by applying tilt angles as an additional control input to outperform the underactuated system. These aerial robots can even hover at vertical attitude, thus presenting the ability to pass through any inclined narrow gaps. However, the task of passing through a small circle hole or pit is still a great challenge, because the widths of these robots are unclear. Our work draws inspiration from the ability of a snake to pass through a small hole by changing its shape.

Such an aerial transformation requires a multilinked structure and offers an advantage for another high-level application, namely, aerial manipulation. Generally, aerial manipulation is achieved by combining traditional multirotors and arm-manipulators (e.g., [11]–[13]), thus permitting a wide workspace of the end-effector ($\mathsf{SE}(3)$). However, a great challenge exists for integrated aerial systems—the large load imposed on the control of multirotor attitude by the moment generated by manipulator gravity. Therefore, a further motivation of our work is the distribution of such load and the design of the link structure where the rotor is embedded.

Manuscript received September 10, 2017; accepted January 2, 2018. Date of publication January 15, 2018; date of current version February 8, 2018. This letter was recommended for publication by Associate Editor V. Lippiello and Editor J. Roberts upon evaluation of the reviewers' comments. *(Corresponding author: Moju Zhao.)*

The authors are with the Department of Mechano-Infomatics, The University of Tokyo, Tokyo 113-8656, Japan (e-mail: chou@jsk.t.u-tokyo.ac.jp; anzai@jsk.imi.i.u-tokyo.ac.jp; shifan@jsk.imi.i.u-tokyo.ac.jp; xychen@jsk.imi.i.u-tokyo.ac.jp; k-okada@jsk.t.u-tokyo.ac.jp; inaba@i.u-tokyo.ac.jp).

Digital Object Identifier 10.1109/LRA.2018.2793344

In this letter, we introduce a novel aerial robot with the ability of multi-DoF aerial transformation (Fig. 1). In our previous work [14], a multirotor with 2D multilinks has been developed. Given that all rotor disks are aligned in the same plane, the previous transformable aerial robot is underactuated, thus resulting in the appearance of uncontrollable forms called singular forms. The existence of singular forms might limit the valid range of aerial transformation, thus causing invalid solution in terms of the transformation path. Therefore, an original 2DoF force vectoring apparatus called the dual-rotor gimbal module is designed for our new transformable aerial robot. Although such an overactuated design leads to mechanical complexity, the redundancy of actuators can render two following advantages: a) the decrease of the singular form region; b) the extension of the feasible volume of the total force and moment generated by the aerial robot. The former benefits tasks that are associated with the problem of path planning (e.g., passing gap or hole), whereas the latter enhances robustness against steady turbulence and benefits the motion involving physical interaction (e.g., aerial manipulation task). These two advantages will be discussed in detail in Section II.

The multilinked structure results in the variable rotor configuration and the relative movement of the center of gravity (CoG) with regard to the root link. Referring to related investigations on the models with the variable CoG, different moving mass control methods are proposed to achieve the attitude control for coaxial helicopter [15] and quadrotor [16] that have mechanisms for moving a certain weight. However, such a mechanism requires an additional weight and is unsuitable for a multilinked structure. Hence, in this work, a decoupled control method is developed to achieve the stability in full pose $\mathsf{SE}(3)$ (6DoF) with the variable rotor configuration. This control method can be divided into two parts: the thrust force control and the rotor gimbal (vectoring) control.

This letter presents the design and control method for DRAGON. Section II shows the mechanical design and derives the variable rotor configuration. Section III shows the dynamics of the whole multilinked structure on the basis of the special definition of the orientation of the multilinks $\{CoG\}$ frame. Section IV reveals the decoupled control system for the 6DoF pose of the $\{CoG\}$ frame under the desired multilinks form. Finally, Section V presents the prototype platform and related experimental results to demonstrate the feasibility of the multi-DoF aerial transformation.

II. Design

A. Thrust Rotor Module

To achieve an arbitrary 6DoF pose in the air, rotor disks cannot be aligned in the same plane, which is the case for traditional multirotors. In terms of rotor alignment, existing approaches include the following: a) fixed rotor configuration with different tilt directions (e.g., [6], [7], [17]); b) each rotor module actuated by a single servo motor to achieve 1DoF tilting (e.g., [9], [10], [18]); c) each rotor module actuated by two servo motors to achieve 2DoF tilting (e.g., [19]).

In this work, we apply the 2DoF vectoring mechanism to maximize the advantages of the overactuated system, and define it as the gimbal module, referring to the ability to make the rotor disk level towards the ground. The sufficient stiffness of the link structure against bending and twisting is crucial. Otherwise, bending/twisting vibration would occur and greatly affect the control stability. Hence, a rigid and lightweight rod pipe made from carbon fiber is employed. To achieve the 2DoF vectoring mechanism with rod structure, the rotor should be arranged at the sides of the rod, thus indicating that two rotors should exist at both sides to keep the symmetry. Therefore, the dual-rotor gimbal module is designed (see Fig. 2(b)).

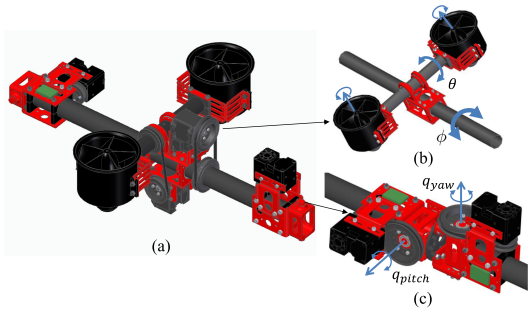

Fig. 2. Mechanical design. (a) Link unit. (b) Dual-rotor gimbal module. (c) Two-DoF joint module.

The dual-rotor gimbal module has the first rotating axis φ around the main rod and the second axis θ around the dual-rotor connection rod. The paired rotors have the same rotation speed but opposite rotation directions. Although such dual-rotor structure is redundant, the property of the counter rotation has two advantages in regard to modeling and control. First, the opposite drag moments generated by paired rotors counteract each other. Second, the gyroscopic moments generated by tilting the rotating propeller can counteract each other as well. To guarantee the performance of servo control for force vectoring, the rotational inertia of the gimbal module should be as small as possible. Therefore, a small rotor with a ducted fan is applied because of the small size and relatively high power (e.g., [20]).

B. Two-DoF Joint Module

As shown in Fig. 2(c), the composite 2DoF joint module consists of two identical single joint structures and an inter connection part. The two rotation axes are orthogonal and rotating angles q_{yaw} and q_{pitch} are constrained within $[-\frac{\pi}{2}, \frac{\pi}{2}]$. Given that the joint is actuated by a servo motor, the joint stiffness is associated with the power of the servo motor. However, most of the small and commercially available servo motors are power limited. In most hovering cases, the form of multilinks is fixed. In other words, multilinks are expected to perform as a rigid body in such a situation. However, the turbulence or the periodic control input may cause vibrations at the joint part and violate the rigid condition. Hence, a pulley mechanism is applied to amplify the servo torque to decrease back-drivability, i.e., the mechanical compliance against such vibrations.

C. Variable Rotor Configuration

On the basis of the skeleton model (see Fig. 3), forward kinematics using joint angles $\boldsymbol{q} \in \mathcal{R}^{2(N-1)}$ from the root (first) link can be performed. Regarding the root link frame $\{L_1\}$ as the reference frame, the rotor position ${}^{\{L_1\}}\boldsymbol{p}_i$ can be retrieved recursively, and then the center of gravity of multilinks ${}^{\{L_1\}}\boldsymbol{r}_{\{CoG\}}$ (which is the origin of the frame $\{CoG\}$) can be calculated. It is obvious that these positions can be treated as functions of joint angles $\boldsymbol{q}$. However, for modeling and control, rotor positions should be described in the frame $\{CoG\}$. Hence, it is necessary to define the orientation of the frame $\{CoG\}$ first. Theoretically, the orientation of the frame $\{CoG\}$ is arbitrary and generally coincides with the root link frame $\{L_1\}$. On the other hand, in a real situation, the estimated attitude w.r.t. the world frame $\{W\}$ is first obtained on the frame of the flight controller (embedded

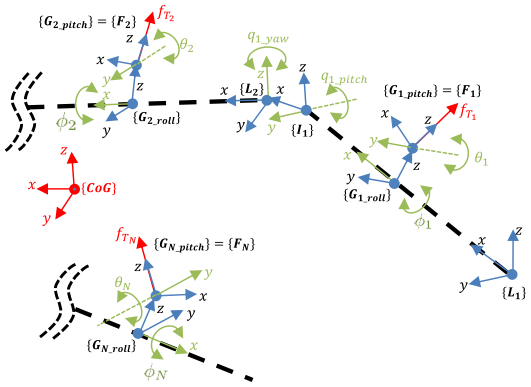

Fig. 3. Skeleton model of DRAGON demonstrating kinematics and rotor configuration. The green arrows indicate the rotation axes associated with both joint angles (q_{i_yaw}, q_{i_pitch}) and gimbal tilt angles (θ_i, ϕ_i). The origin of the frame $\{CoG\}$ is the center of gravity of the multilinked structure.

with the IMU unit). The link attached with the flight controller is called the baselink. For convenience at this point, the orientation of the frame $\{CoG\}$ is defined to be identical with the orientation of baselink frame $\{B\}$; an improved definition will be introduced later in Section III for flight control. Hence the rotor position ${}^{\{CoG\}}\boldsymbol{p}_i$ expressed in the frame $\{CoG\}$ can be calculated by straightforward transformation.

On the other hand, the vectored thrust force ${}^{\{CoG\}}\boldsymbol{f}_i$ w.r.t. the frame $\{CoG\}$ can be given by

$$ {}^{\{CoG\}}\boldsymbol{f}_i = f_{T_i}\,{}^{\{CoG\}}\boldsymbol{b}_i = f_{T_i}\,{}^{\{CoG\}}R_{\{L_i\}}(\boldsymbol{q})\,{}^{\{L_i\}}R_{\{F_i\}}(\theta_i,\phi_i)\boldsymbol{b} \tag{1} $$

Vectored thrust force ${}^{\{CoG\}}\boldsymbol{f}_i$ can be divided into the norm f_{T_i} and normal vector ${}^{\{CoG\}}\boldsymbol{b_i}$. Further derivation is performed by decomposing ${}^{\{CoG\}}\boldsymbol{b_i}$ into three parts. ${}^{\{CoG\}}R_{\{L_i\}}$ denotes the orientation of the link frame $\{L_i\}$ w.r.t. the frame $\{CoG\}$ containing joint angles $\boldsymbol{q}$ as variables. ${}^{\{L_i\}}R_{\{F_i\}}$ indicates the orientation of the rotor disk frame $\{F_i\}$ w.r.t. the link frame $\{L_i\}$ containing 2DoF tilt angles (θ_i , ϕ_i). $\boldsymbol{b} = (\,0\;0\;1\,)^{\mathrm{T}}$ is the constant unit vector. It can be noted that the drag torque caused by the propeller rotation is omitted because of the counteraction by the counter rotation of the proposed dual-rotor module. The moment generated by the thrust force around the origin of the frame $\{CoG\}$ can be written as:

$$ {}^{\{CoG\}}\boldsymbol{\tau}_i = {}^{\{CoG\}}\boldsymbol{p}_i \times {}^{\{CoG\}}\boldsymbol{f}_i \tag{2} $$

Finally, the total force and torque can be summarized as

$$ \begin{pmatrix} {}^{\{CoG\}}\boldsymbol{f} \\ {}^{\{CoG\}}\boldsymbol{\tau} \end{pmatrix} = \begin{pmatrix} \sum_{i=1}^{N} {}^{\{CoG\}}\boldsymbol{f}_i \\ \sum_{i=1}^{N} {}^{\{CoG\}}\boldsymbol{p}_i \times {}^{\{CoG\}}\boldsymbol{f}_i \end{pmatrix} = \begin{pmatrix} B \\ P\times B \end{pmatrix} \boldsymbol{f}_T = M\boldsymbol{f}_T $$

$$ B = \begin{pmatrix} {}^{\{CoG\}}\boldsymbol{b}_1 & {}^{\{CoG\}}\boldsymbol{b}_2 & \cdots & {}^{\{CoG\}}\boldsymbol{b}_N \end{pmatrix}; $$

$$ P = \begin{pmatrix} {}^{\{CoG\}}\boldsymbol{p}_1 & {}^{\{CoG\}}\boldsymbol{p}_2 & \cdots & {}^{\{CoG\}}\boldsymbol{p}_N \end{pmatrix} $$

$$ \boldsymbol{f}_T = \begin{pmatrix} f_{T_1} & f_{T_2} & \cdots & f_{T_N} \end{pmatrix}^{\mathrm{T}} \tag{3} $$

where the i-th column of $P \times B$ is defined to be ${}^{\{CoG\}}\boldsymbol{p}_i \times {}^{\{CoG\}}\boldsymbol{b}_i$.

Configuration matrix M varies because of joint angles $\boldsymbol{q}$, thus indicating the variable rotor configuration. Matrix M is also influenced by the control input of rotor tilt angles $\boldsymbol{\varphi} \in \mathcal{R}^N$ and $\boldsymbol{\theta} \in \mathcal{R}^N$. As mentioned above, such an overactuated system has two advantages: the decrease of the singular form region and the increase of total force and moment volume. The singular form appears when the rank of matrix M decreases (see [14]). However, the proposed 2DoF vectoring mechanism can influence most of the components in this matrix, thus indicating that the modification of tilt angles can greatly prevent the matrix from rank decrease. Referring to the second advantage, we focus on the mapping from thrust force $\boldsymbol{f}_T$ to total force ${}^{\{CoG\}}\boldsymbol{f}$ and moment ${}^{\{CoG\}}\boldsymbol{\tau}$ by matrix M. Given that matrix components are variable, the mapping region (volume) in such an overactuated system is much larger than the case of the aerial robot with fixed rotor configuration, thus leading to higher robustness towards turbulence and better performance on the aerial manipulation than the aforementioned integrated aerial systems (e.g., [11]).

III. Dynamics

A. Orientation of the CoG Frame

The orientation of the frame $\{CoG\}$ w.r.t. the world frame $\{W\}$ is defined as ${}^{\{W\}}R_{\{CoG\}} \in \mathsf{SO}(3)$, and the relationship between the orientation and angular velocity of the frame $\{CoG\}$ can be described as ${}^{\{W\}}\dot{R}_{\{CoG\}} = {}^{\{W\}}R_{\{CoG\}}\,{}^{\{CoG\}}\boldsymbol{\omega}_{\{CoG\}}$. Although the rotational dynamics directly expressed on $\mathsf{SO}(3)$ and related nonlinear feedback control have been proposed in [21], the nonlinearity would increase the complexity on the proposed multilinked structure because of the force vectoring mechanism. Therefore, the Z-Y-X Euler angles (Ψ, Θ, Φ) are introduced to help to linearize the dynamics, and the following definition on the orientation of the baselink frame $\{B\}$ w.r.t the frame $\{CoG\}$ is proposed:

$$ {}^{\{CoG\}}R_{\{B\}} = R_Y(\Theta_d)R_X(\Phi_d) \tag{4} $$

where, Θ_d, Φ_d denote the desired Euler angles. If the baselink frame $\{B\}$ is desired to hold at the orientation of $(\Psi_d, \Theta_d, \Phi_d)$ expressed in the world frame $\{W\}$, the rotation matrix of the frame $\{CoG\}$ w.r.t the world frame $\{W\}$ would be equal to $R_Z(\Psi_d)$ which is the level orientation, because of ${}^{\{W\}}R_{\{CoG\}} = {}^{\{W\}}R_{\{B\}}\,{}^{\{CoG\}}R^{\mathrm{T}}_{\{B\}}$. Therefore, the desired orientation of the frame $\{CoG\}$ should be always horizontal. The Z-Y-X Euler angles of the frame $\{CoG\}$ are redefined as a vector ${}^{\{W\}}\boldsymbol{\alpha}_{\{CoG\}} = (\,\Phi_{CoG}\;\Theta_{CoG}\;\Psi_{CoG}\,)^{\mathrm{T}}$. The following approximation near the horizontal attitude is available:

$$ {}^{\{W\}}\dot{\boldsymbol{\alpha}}_{\{CoG\}} \approx {}^{\{CoG\}}\boldsymbol{\omega}_{\{CoG\}} \tag{5} $$

B. Approximation to the Rigid Body

On the basis of the well-defined CoG frame described above, the dynamics of the proposed multilinked robot can be written as follows:

$$ \begin{aligned} \sum_{i=1}^{N_s} m_{s_i}\,{}^{\{W\}}\ddot{\boldsymbol{r}}_{s_i} &= m_{\sum}\,{}^{\{W\}}\ddot{\boldsymbol{r}}_{\{CoG\}} \\ &= {}^{\{W\}}R_{\{CoG\}}\,{}^{\{CoG\}}\boldsymbol{f} - m_{\sum}\boldsymbol{g} \end{aligned} \tag{6} $$

$$ {}^{\{CoG\}}\dot{\mathcal{L}}_{\sum} = \sum_{i=1}^{N_s} {}^{\{CoG\}}\dot{\mathcal{L}}_{s_i} = {}^{\{CoG\}}\boldsymbol{\tau} \tag{7} $$

where, ${}^{\{CoG\}}\boldsymbol{f}$ and ${}^{\{CoG\}}\boldsymbol{\tau}$ are the total wrench described in (3). $m_{\sum}$ and ${}^{\{CoG\}}\mathcal{L}_{\sum}$ are the total mass and angular momentum of

the multilinked structure, respectively. Symbol "s" stands for "segment" in multilinks, including the fixed part of the link unit with local frame $\{L_i\}$, the dual-rotor gimbal roll module with local frame$\{G_{i,roll}\}$, the dual-rotor gimbal pitch module with local frame$\{G_{i,pitch}\}$, and the joint inter connector module with local frame $\{I_i\}$.

The individual angular momentum ${}^{\{CoG\}}\mathcal{L}_{s_i}$ can be further written as the combination of the offset from the origin of the frame $\{CoG\}$ to the link mass center and segment inertia term:

$$\begin{aligned}{}^{\{CoG\}}\mathcal{L}_{s_i} &= {}^{\{CoG\}}\boldsymbol{p}_{s_i} \times (m_{s_i}{}^{\{CoG\}}\dot{\boldsymbol{p}}_{s_i}) \\ &\quad + {}^{\{CoG\}}R_{\{s_i\}} I_{s_i} {}^{\{CoG\}}R_{\{s_i\}}^{\mathrm{T}} {}^{\{CoG\}}\boldsymbol{\omega}_{\{s_i\}} \end{aligned} \tag{8}$$

where ${}^{\{CoG\}}R_{\{s_i\}}$ is the rotation matrix of the i-th segment frame $\{S_i\}$ w.r.t. the frame $\{CoG\}$, and I_{s_i} is the constant inertia tensor expressed in the local frame $\{S_i\}$. Furthermore, ${}^{\{CoG\}}\boldsymbol{p}_{s_i}$ is the position of the mass center of the i-th segment w.r.t. the frame $\{CoG\}$. ${}^{\{CoG\}}\boldsymbol{\omega}_{\{s_i\}}$ is the angular velocity of the i-th segment expressed in the frame $\{CoG\}$, containing the angular velocity ${}^{\{CoG\}}\boldsymbol{\omega}_{\{CoG\}}$, the joint angles vector $\boldsymbol{q}$ and the joint velocity vector $\dot{\boldsymbol{q}}$ as variables.

Although further derivation can be obtained by substituting (8) into (7), the derivative terms (i.e., ${}^{\{CoG\}}\dot{\boldsymbol{\omega}}_{\{CoG\}}$, $\dot{\boldsymbol{q}}$) and the second derivative term (i.e., $\ddot{\boldsymbol{q}}$) should be involved, thus bringing high complexity to the later control method. Therefore a crucial assumption is proposed in this work to simplify the dynamics, i.e., all joints are actuated slowly. Thus, the joint velocity can be considered zero, resulting in the following approximation: ${}^{\{CoG\}}\boldsymbol{\omega}_{\{s_i\}} \approx {}^{\{CoG\}}\boldsymbol{\omega}_{\{CoG\}}$. Subsequently, (7) can be simplified as follows:

$${}^{\{CoG\}}I_{\sum}{}^{\{CoG\}}\dot{\boldsymbol{\omega}}_{\{CoG\}} + {}^{\{CoG\}}\boldsymbol{\omega}_{\{CoG\}} \times {}^{\{CoG\}}I_{\sum}{}^{\{CoG\}}\boldsymbol{\omega}_{\{CoG\}} = {}^{\{CoG\}}\boldsymbol{\tau} \tag{9}$$

$${}^{\{CoG\}}I_{\sum} = \sum_{i=1}^{N_s} I_{s_i}^{'} = \sum_{i=1}^{N_s} (m_{s_i}{}^{\{CoG\}}\hat{\boldsymbol{p}}_{s_i}{}^{\{CoG\}}\hat{\boldsymbol{p}}_{s_i}^{\mathrm{T}} + {}^{\{CoG\}}R_{\{s_i\}} I_{s_i} {}^{\{CoG\}}R_{\{s_i\}}^{\mathrm{T}}) \tag{10}$$

Note that the hat map $\wedge$ transforms a vector in $\mathcal{R}^3$ to a 3×3 skew-symmetric matrix.

By using the approximation of (5), the rotational dynamics (9) can be further linearized as follows:

$${}^{\{CoG\}}I_{\sum}{}^{\{W\}}\ddot{\boldsymbol{\alpha}}_{\{CoG\}} = {}^{\{CoG\}}\boldsymbol{\tau} \tag{11}$$

The second term in (9) is omitted because the square term of ${}^{\{CoG\}}\boldsymbol{\omega}_{\{CoG\}}$ is considerably small near the stable point. Eventually, after integrating with the rotor configuration of (3), the whole dynamics can be summarized as follows:

$$\begin{aligned} &\ddot{\boldsymbol{x}} = Q\boldsymbol{f}_T - \boldsymbol{G} \\ &\boldsymbol{x} = \begin{pmatrix} {}^{\{W\}}\boldsymbol{r}_{\{CoG\}} & {}^{\{W\}}\boldsymbol{\alpha}_{\{CoG\}} \end{pmatrix}^{\mathrm{T}}; \\ &Q = \begin{pmatrix} \frac{1}{m_\Sigma} R_Z({}^{\{W\}}\alpha_z) B(\boldsymbol{\theta}, \boldsymbol{\phi}) & I_\Sigma^{-1} P \times B(\boldsymbol{\theta}, \boldsymbol{\phi}) \end{pmatrix}^{\mathrm{T}} \end{aligned} \tag{12}$$

where the configuration matrix B is represented as a function of gimbal tilt angles $(\boldsymbol{\theta}, \boldsymbol{\phi})$. Also note that ${}^{\{W\}}R_{\{CoG\}}$ in (6) is approximated as $R_Z({}^{\{W\}}\alpha_z)$ near the equilibrium point. $\boldsymbol{G}$ is the constant term associated with gravity.

Consequently, on the basis of the assumption of slow transforming, the multilinked model in this work can considered a single rigid body with variable inertial parameters.

IV. Control

Nonlinearity still exists at the right side of (12), including the trigonometric function about gimbal tilt angles $(\boldsymbol{\theta}, \boldsymbol{\phi})$ as expressed in (1), along with the multiplication among tilt angles and the thrust force $\boldsymbol{f}_T$. As an efficient solution in [22], ${}^{\{CoG\}}\boldsymbol{f}_i$ in (1) is considered the alternative control input to linearize the control model. Subsequently, the gimbal tilt angles and thrust force are allocated by a simple geometric rule. The key feature of the feedback control, as described in [22], is the usage of pseudo inverse matrix to achieve the non-interfered control, thus implying that the valid range of the thrust force is not taken into account and saturation may occur. Thus, in this work, we propose a new control method that decouples the thrust force control and rotor gimbal control to guarantee the optimal regulator for thrust force.

A. Thrust Force Control Based on Linear-Quadratic-Integral

Given that the desired orientation of the frame $\{CoG\}$ is level $({}^{\{W\}}R_{\{CoG\},d} = R_Z(\Psi_d))$, one of the candidates to achieve hovering state is ${}^{\{CoG\}}\boldsymbol{f}_{i,d} = \begin{pmatrix} 0 & 0 & f_{T_i,d} \end{pmatrix}^{\mathrm{T}}$, that is, to find target gimbal tilt angles $(\theta_{i,d}, \phi_{i,d})$ to satisfy the following constraint:

$${}^{\{CoG\}}R_{\{F_i\}} = {}^{\{CoG\}}R_{\{B\}}{}^{\{B\}}R_{\{L_i\}}(\boldsymbol{q}){}^{\{L_i\}}R_{\{F_i\}}(\theta_{i,d}, \phi_{i,d}) = R_Z(\lambda) \tag{13}$$

where subscript d denotes the desired value and ${}^{\{CoG\}}R_{\{B\}}$ corresponds to (4). Note that $R_Z(\lambda)$ indicates that the frame $\{F_i\}$ is level w.r.t. the frame $\{CoG\}$. Subsequently, the following equilibrium is available at the target stable point.

$$\sum_{i=1}^{N} \boldsymbol{f}_T = m_\Sigma \boldsymbol{g} \tag{14}$$

In our previous work [14], the linear-quadratic-integral (LQI) optimal control method [23] is proposed to minimize the force norm and avoid the force saturation based on the equilibrium (14). Given that the thrust force only has influence on three states, namely, ${}^{\{W\}}r_z$, ${}^{\{W\}}\alpha_x$, ${}^{\{W\}}\alpha_y$, the extended states in LQI framework can be written as $\boldsymbol{x}^{'} = \begin{pmatrix} {}^{\{W\}}r_z & {}^{\{W\}}\dot{r}_z & {}^{\{W\}}\alpha_x & {}^{\{W\}}\dot{\alpha}_x & {}^{\{W\}}\alpha_y & {}^{\{W\}}\dot{\alpha}_y \end{pmatrix}^{\mathrm{T}}$. Thereafter, the extended state equation can be written as follows:

$$\dot{\boldsymbol{x}}^{'} = A\boldsymbol{x}^{'} + B\boldsymbol{f}_T + \boldsymbol{d} \tag{15}$$

$$\begin{aligned} &\boldsymbol{y} = C\boldsymbol{x}^{'} \\ &\boldsymbol{y} = \begin{pmatrix} {}^{\{W\}}r_z & {}^{\{W\}}\alpha_x & {}^{\{W\}}\alpha_y \end{pmatrix}^{\mathrm{T}}; \\ &B = \begin{pmatrix} \mathbf{0} & Q(3)^{\mathrm{T}} & \mathbf{0} & Q(4)^{\mathrm{T}} & \mathbf{0} & Q(5)^{\mathrm{T}} \end{pmatrix}^{\mathrm{T}} \end{aligned} \tag{16}$$

where, $Q(i)$ denotes the i-th row vector of the matrix Q in (12), and $\boldsymbol{d}$ is the constant term (i.e., gravity). The sparse matrix A and C are easily obtained from the equation. The corresponding cost function and feedback control function of LQI control is given as follows

$$J = \int_0^\infty \left(\bar{\boldsymbol{x}}^{\mathrm{T}} W_1 \bar{\boldsymbol{x}} + \tilde{\boldsymbol{f}}^{\mathrm{T}} W_2 \tilde{\boldsymbol{f}} \right) dt \tag{17}$$

$$\begin{aligned} &\boldsymbol{f}_{T,d} = K\bar{\boldsymbol{x}} \\ &\bar{\boldsymbol{x}} = \begin{pmatrix} \tilde{\boldsymbol{x}} & \boldsymbol{v} \end{pmatrix}^{\mathrm{T}}; \tilde{\boldsymbol{x}} \equiv \boldsymbol{x}^{'} - \boldsymbol{x}_s^{'}; \dot{\boldsymbol{v}} \equiv \boldsymbol{y}_d - \boldsymbol{y}; \tilde{\boldsymbol{f}} \equiv \boldsymbol{f}_T - \boldsymbol{f}_{T,s} \end{aligned} \tag{18}$$

where, the subscript "s" denotes the final value at the steady state. Therefore, $\boldsymbol{y}_d$ is identical to a part of $\boldsymbol{x}_s^{'}$ (excluding the

first deviation elements). Note that the second term in (17) corresponds with the minimization of the force norm. Although true feedback control is associated with $\tilde{\boldsymbol{f}}$ (i.e., $\tilde{\boldsymbol{f}} = K\bar{\boldsymbol{x}}$), the integrated function has enough ability to compensate for the steady-state error, such as the effect of gravity on the state ${}^{\{W\}}r_z$ and guarantee the asymptotic stability. Thus, $\boldsymbol{f}_{T,s}$ is neglected in (18).

From a mathematical aspect, the algebra Riccati equation (ARE) is solved by the eigen decomposition of hamilton matrix, which is $\mathcal{R}^{6n\times 6n}$ for state $\boldsymbol{x} \in \mathcal{R}^n$. Furthermore, ARE requires to be solved in real time, because the change of joint angles vector makes the matrix Q variant. In the case of an onboard processor, the above process is considerably difficult to execute for whole states ($n = 6$). Thus, the minimum number of states $({}^{\{W\}}r_z, {}^{\{W\}}\alpha_x, {}^{\{W\}}\alpha_y)$ are selected in the LQI framework to optimally control the thrust force.

B. Rotor Gimbal Control

As discussed above, the states other than $({}^{\{W\}}r_z, {}^{\{W\}}\alpha_x, {}^{\{W\}}\alpha_y)$ are not able to be controlled by the thrust force. Therefore, the purpose of rotor gimbal control here is to achieve the stabilization about reset states without preventing the asymptotic stability of the above thrust control at the same time. Assuming that the i-th gimbal module can generate small horizontal force ${}^{\{CoG\}}\boldsymbol{f}_{g_i} \in \mathcal{R}^2$ around the stable state subject to $\|{}^{\{CoG\}}\boldsymbol{f}_{g_i}\| \ll f_{T_i,d}$, the desired vectored force can be rewritten as follows with the derived approximation of $\|{}^{\{CoG\}}\boldsymbol{f}_{i,d}\| \approx f_{T_i,d}$:

$$ {}^{\{CoG\}}\boldsymbol{f}_{i,d} = \left({}^{\{CoG\}}f_{g_i,d}(0)\ {}^{\{CoG\}}f_{g_i,d}(1)\ f_{T_i,d} \right)^{\mathrm{T}} \tag{19}$$

After substituting (19) into (3) and using (12), the dynamics associated with gimbal control can be derived as follows,

$$\ddot{\boldsymbol{x}}'' = H\boldsymbol{f}_g = \begin{pmatrix} H_1 \\ H_2 \end{pmatrix} \boldsymbol{f}_g$$

$$\boldsymbol{x}'' = \left({}^{\{W\}}r_x\ {}^{\{W\}}r_y\ {}^{\{W\}}\alpha_x\ {}^{\{W\}}\alpha_y\ {}^{\{W\}}\alpha_z \right)^{\mathrm{T}}$$

$$\boldsymbol{f}_g = \left({}^{\{CoG\}}\boldsymbol{f}_{g1}^{\mathrm{T}}\ {}^{\{CoG\}}\boldsymbol{f}_{g2}^{\mathrm{T}}\ \cdots\ {}^{\{CoG\}}\boldsymbol{f}_{gN}^{\mathrm{T}} \right)^{\mathrm{T}}$$

$$H_1 = \frac{R_Z({}^{\{W\}}\alpha_z)}{m_\Sigma} \begin{pmatrix} 1\ 0\ 1\ 0\ \cdots\ 1\ 0 \\ 0\ 1\ 0\ 1\ \cdots\ 0\ 1 \end{pmatrix}$$

$$H_2 = I_\Sigma^{-1} \begin{pmatrix} 0 & -{}^{\{CoG\}}p_{1_z} & 0 & -{}^{\{CoG\}}p_{2_z} \cdots & 0 & -{}^{\{CoG\}}p_{N_z} \\ {}^{\{CoG\}}p_{1_z} & 0 & {}^{\{CoG\}}p_{2_z} & 0 & \cdots\ {}^{\{CoG\}}p_{N_z} & 0 \\ -{}^{\{CoG\}}p_{1_y} & {}^{\{CoG\}}p_{1_x} & -{}^{\{CoG\}}p_{2_y} & {}^{\{CoG\}}p_{2_x} & \cdots -{}^{\{CoG\}}p_{N_y} & {}^{\{CoG\}}p_{N_x} \end{pmatrix} \tag{20}$$

where ${}^{\{CoG\}}p_i$ corresponds with (2). Similar to (12), the influence of ${}^{\{W\}}\alpha_x$ and ${}^{\{W\}}\alpha_y$ are neglected in matrix H_1 because the attitude of the $\{CoG\}$ frame is assumed to be almost around the stable point.

Although the same LQI framework can be applied for the above state equation, the states are 5DoF, thus resulting in the 30×30 hamilton matrix to be solved in ARE. Therefore, noninterference feedback control associated with the general pseudo inverse is developed.

$$\boldsymbol{f}_{g,d} = H^{\dagger}\ddot{\boldsymbol{x}}_d'' \tag{21}$$

$$\ddot{\boldsymbol{x}}_d'' = \boldsymbol{k}_P\left(\boldsymbol{x}_d'' - \boldsymbol{x}''\right) + \boldsymbol{k}_I \int \left(\boldsymbol{x}_d'' - \boldsymbol{x}''\right) d\tau - \boldsymbol{k}_D\dot{\boldsymbol{x}}'' \tag{22}$$

$$H^{\dagger} = H^{\mathrm{T}}(HH^{\mathrm{T}})^{-1} \tag{23}$$

where PID gain vectors $\boldsymbol{k}_P$, $\boldsymbol{k}_I$, and $\boldsymbol{k}_D$ are carefully chosen to achieve asymptotically stability around the desired state $\boldsymbol{x}_d''$. Note that the desired values for ${}^{\{W\}}\alpha_{x,d}$ and ${}^{\{W\}}\alpha_{y,d}$ are zero because the desired orientation for the frame $\{CoG\}$ is level. The desired value ${}^{\{W\}}\alpha_{z,d}$ is equal to Ψ_d.

If any one of ${}^{\{CoG\}}p_{i_z}$ is not zero, ${}^{\{W\}}\alpha_x$ and ${}^{\{W\}}\alpha_y$ would be influenced by both the thrust force control and the rotor gimbal one. However, the hybrid control for those two states can still achieve asymptotic stability for the desired horizontal attitude because of the property of linear control system. On the other hand, if every ${}^{\{CoG\}}p_{i_z}$ is equal to zero, the gimbal control would not influence the roll/pitch rotational motion and the rank of matrix H would not be full. Therefore, we define the following controllability for ${}^{\{W\}}\alpha_x$ and ${}^{\{W\}}\alpha_y$:

$$\kappa(\boldsymbol{q}, \Phi_d, \Theta_d) = \sqrt{det(HH^{\mathrm{T}})} \tag{24}$$

If $\kappa(\boldsymbol{q}, \Phi_d, \Theta_d)$ is smaller than a certain threshold (e.g., 1e-3), the influence of gimbal control on ${}^{\{W\}}\alpha_x$ and ${}^{\{W\}}\alpha_y$ is neglected. New matrix $H' = \left(H_1^{\mathrm{T}}\ H_2(3)^{\mathrm{T}} \right)^{\mathrm{T}}$ is chosen to design the same control framework for reset states. Note that $H_2(3)$ stands for the third row vector of H_2.

The gimbal control model is overactuated and the DoF is twice of that of thrust force control model. Thus, the pseudo inverse matrix can guarantee asymptotic stability without large control feedback value. Furthermore, the pseudo inverse method is associated with minimizing the required control effort under the noninterference condition. Compared with the rotor gimbal control, the thrust force control is more crucial because of the necessity to balance with gravity.

Assuming that the dual-rotor gimbal module is well actuated by servo motors, the fundamental input in terms of rotor gimbal control are the target gimbal tilt angles $(\theta_{i,d}, \phi_{i,d})$. By integrating (1), (13), and (19), the gimbal tilt angles θ_i and ϕ_i can be obtained as follows:

$$\begin{pmatrix} \sin(\theta_i) \\ -\sin(\phi_i)\cos(\theta_i) \\ \cos(\phi_i)\cos(\theta_i) \end{pmatrix}^{\mathrm{T}} = {}^{\{B\}}R_{\{L_i\}}(\boldsymbol{q})^{\mathrm{T}}\,{}^{\{CoG\}}R_{\{B\}}^{\mathrm{T}}\,{}^{\{CoG\}}\boldsymbol{b}_i = \boldsymbol{b}_i' \tag{25}$$

$$\phi_i = \tan^{-1}(-\boldsymbol{b}_i'(1), \boldsymbol{b}_i'(2)) \tag{26}$$

$$\theta_i = \tan^{-1}(\boldsymbol{b}_i'(0), -\boldsymbol{b}_i'(1)\sin(\phi_i) + \boldsymbol{b}_i'(2)\cos(\phi_i)) \tag{27}$$

Note that $f_{T_i,d}$ in (13) is calculated from the LQI control method ((18)). However, signal noise and mechanical vibration would make more effect on attitude estimation and control than position estimation and control, which can be considered unnecessary perturbation around the stable state. Therefore, instead of $f_{T_i,d}$, only the components about altitude motion (i.e ${}^{\{W\}}r_z, {}^{\{W\}}\dot{r}_z$) in (18) are extracted to be considered the third component of ${}^{\{CoG\}}\boldsymbol{f}_{i,d}$ because the rest terms should be convergent to zero theoretically.

While combining the rotor gimbal control with the former thrust force control, the inertia tensor of gimbal related segment ${}^{\{CoG\}}I'_{gimbal_i}$ w.r.t. the frame $\{CoG\}$ would vary because of gimbal tilting. The perturbation of target angles $(\theta_{i,d}, \phi_{i,d})$ are relatively small from the value at stable state $(\theta_{i,s}, \phi_{i,s})$. Furthermore, the individual inertia of a gimbal-related segment is not as large as other segments. Therefore, the inertia tensor can be approximated as the constant value ${}^{\{CoG\}}I'_{gimbal_i}(\theta_{i,s}, \phi_{i,s})$ in the former thrust force control.

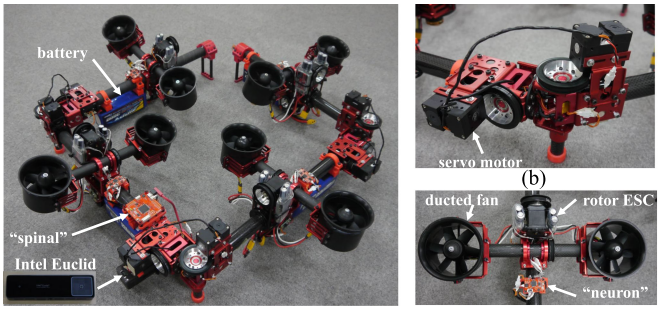

Fig. 4. (a) Snapshot of the prototype comprising four links. The original FCU with onboard IMU unit called "spinal" and high-level processor Intel Euclid are attached to the second link, which is defined as the baselink. (b) Two-DoF joint module with commercially available servo motors. (c) Dual-rotor gimbal module: the original distributed board called "neuron" attached to each link unit, and dual ducted fan rotor controlled by the electronic speed controllers (ESCs).

TABLE I
MAIN SPECIFICATION

Component	Description
Link unit	0.424 [m]
Lipo battery unit	22.2 [V], 3000 [mAh]
Ducted fan rotor	70 [mm], 2200 [KV] max 13 [N]
Gimbal servo motor	Dynamixel MX28AR pulley ratio 1:1
Joint servo motor	Dynamixel XH430-W350R pulley ratio 1:2
Original internal Communication system	CAN protocol

TABLE II
ROBOT MASS BREAKDOWN

Segment	Qty	Unit Weight [Kg]	Total Weight [Kg]
Link (with battery)	4	0.772 ∼ 1.086 (battery: 0.415)	3.5479
Gimbal roll	4	0.440	1.760
Gimbal pitch	4	0.419	1.676
Joint inter connector	3	0.133	0.399
	Robot		7.38225

V. EXPERIMENTS

A. Prototype Platform

In this work, a quad prototype based on the presented design method is constructed (see Fig. 4). The specification detail is explained in Tables I and II. Fig. 5 shows how onboard processes are executed. The reliable internal communication system has been developed in our previous work [24] to connect the original FCU "spinal" and distributed board "neuron". In regard with the state estimation, the "spinal" utilizes the onboard IMU unit to calculate the angular velocity ${}^{\{CoG\}}\boldsymbol{\omega}_{\{CoG\}}$ and orientation ${}^{\{W\}}\boldsymbol{\alpha}$ except the yaw angle because the magnetometer has low accuracy in the indoor environment. By combining the motion capture system with the kinematics information, the position ${}^{\{W\}}\boldsymbol{r}_{\{CoG\}}$, velocity ${}^{\{W\}}\dot{\boldsymbol{r}}_{\{CoG\}}$ and yaw angle ${}^{\{W\}}\alpha_z$ are estimated for the flight control system. The joint angles are first

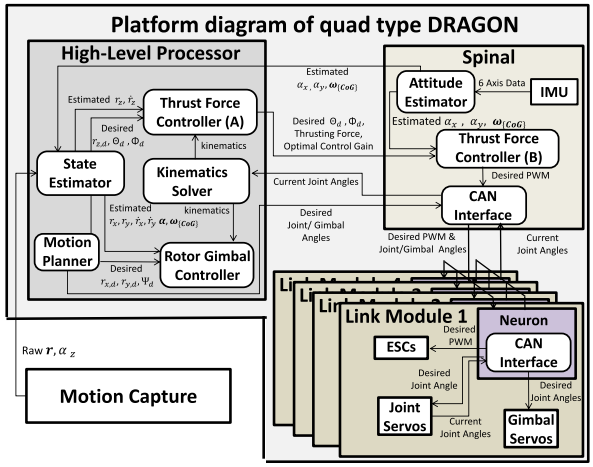

Fig. 5. The platform diagram for the quad-type DRAGON. All the symbols (without superscript $\{W\}$) correspond to the derivation in Section IV. The thrust force controller involves the real-time update for the LQI control gains expressed in (17) and the feedback control calculation expressed in (18). The former process is executed in the high-level processor, i.e., thrust force controller (A); the feedback control calculation associated with r_z is also processed in thrust force controller (A). The rest states are calculated in "spinal" board, i.e., thrust force controller (B).

gathered by each corresponding "neuron", then transmitted to the high-level processor via the "spinal". Note that the tilt angles of the gimbal module are not required to be sent to the high-level processor, since it is not necessary for the rotor gimbal control. The battery unit is distributed at each link unit, and the total capacity is 12000 [mAh] with 22.2 [V], thus leading to the flight time of around 3 [min]. As shown in Fig. 4, the second link attached with flight controller is defined as the baselink. Therefore the desired angles Θ_d, Φ_d denote the orientation of the second link w.r.t. the world frame.

As shown in the Fig. 5, the top inputs to the whole system are as follows: a) the desired position of the CoG frame ${}^{\{W\}}\boldsymbol{r}_d$; b) the desired attitude of the baselink link $(\Psi_d, \Theta_d, \Phi_d)$, where the desired yaw angle Ψ_d is equal to that of the CoG frame; c) the desired form of the multilink structure, i.e., $\boldsymbol{q}_d = (\, q_{1\_pitch}\ q_{1\_yaw}\ q_{2\_pitch}\ q_{2\_yaw}\ q_{3\_pitch}\ q_{3\_yaw}\,)^{\mathrm{T}}$.

In regard to the control gains, the gain matrices in (17) are $W_1 = diag(400, 40, 400, 40, 20, 30, 1, 1, 20)$; $W_2 = I_{4,4}$. The PID gain vectors in (22) are set as $\boldsymbol{k}_P = [18, 18, 20, 20, 10]^{\mathrm{T}}$; $\boldsymbol{k}_I = [0.2, 0.2, 2.0, 2.0, 0.1]^{\mathrm{T}}$; $\boldsymbol{k}_D = [30, 30, 0.5, 0.5, 5]^{\mathrm{T}}$.

B. Hovering Experiment Under Fixed Forms

To evaluate the flight control method presented in Section IV, the stability of hovering under a series of fixed forms is first tested. Fig. 6 shows the result about the representative forms:

a) Spiral-like form:
$\boldsymbol{q} = (\,-0.8\ 1.2\ -0.8\ 1.2\ -0.8\ 1.2\,)^{\mathrm{T}}, (\Psi_d, \Theta_d, \Phi_d) = (0, -0.4, 0.4)$
b) Zigzag-link form:
$\boldsymbol{q} = (\,0\ -1.57\ 0\ 0\ 0\ 1.57\,)^{\mathrm{T}}, (\Psi_d, \Theta_d, \Phi_d) = (0, -0.4, -0.4)$
c) "L"-like form:
$\boldsymbol{q} = (\,0\ 0\ 0\ 0\ 0\ 1.57\,)^{\mathrm{T}}, (\Psi_d, \Theta_d, \Phi_d) = (0, 0, 0)$

The control states for the hovering control are the position ${}^{\{W\}}\boldsymbol{r}_{\{CoG\}}$ and attitude ${}^{\{W\}}\boldsymbol{\alpha}_{\{CoG\}}$. As shown in Fig. 6, some obviously large tracking errors ($>0.2[m]$) referring to the hori-

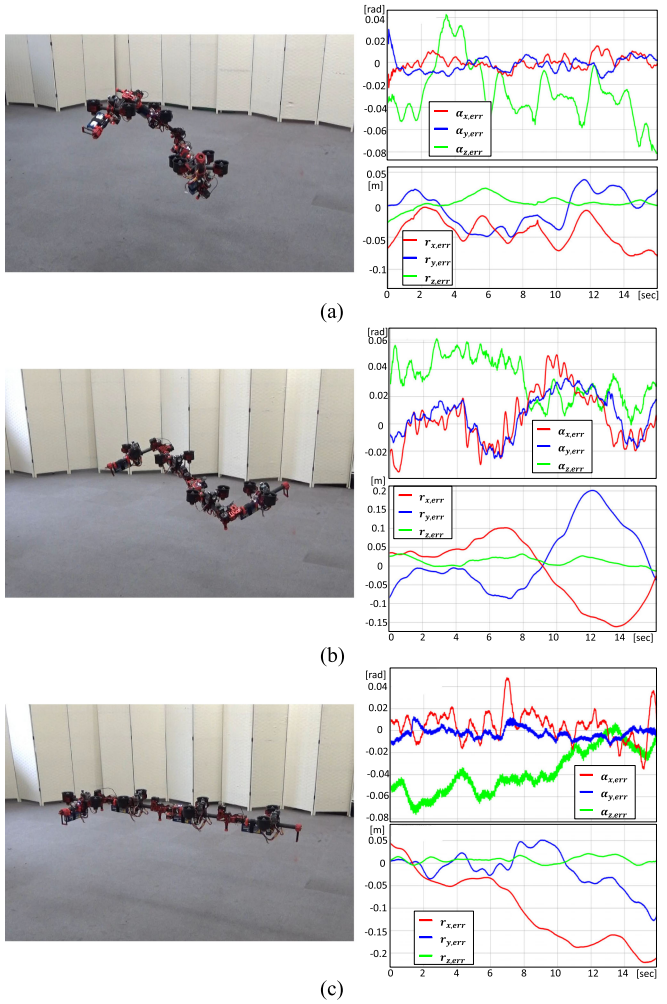

Fig. 6. Hovering snapshots of representative fixed forms with plots of the tracking errors: (a) Spiral-like form, (b) Zigzag-like form, and (c) "L"-like form.

zontal motion ($^{\{W\}}r_x$, $^{\{W\}}r_y$) are observed in form (b) and form (c) respectively. The large error with low frequency in form (b) indicates the weak gimbal PD control. The position $^{\{W\}}\boldsymbol{r}_{\{CoG\}}$ and velocity $^{\{W\}}\dot{\boldsymbol{r}}_{\{CoG\}}$ are obtained by applying LPF to the raw data from motion capture, thus implying that the increase of PD gains would amplify the negative effect of the LPF delay on the dynamics. The sensor fusion method such as [25] is not applied to DRAGON because the mechanical vibration resulted from the gimbal tilting motion considerably influences the performance of the accelerometer inside the IMU unit. As one possible solution in the future, the redundant IMU unit could be implemented on each "neuron" board to support the sensor fusion from all IMU units. The other type of steady-state error in form (c) is associated with the saturation of rotor thrust force. In comparison with the perfect convergent result under the same form in simulation system, the voltage drop of the battery is significant for real machines because the internal resistance cannot be ignored while large currency (e.g., 30 [A]) is flowing. Although the direct solution is to increase the voltage, the battery with more than 6 s (22.2 [V]) and the ESC for such a high voltage are challenging to be commercially available. Although this issue remains for hardware development, the RMS of tacking

TABLE III
RMS TRACKING ERROR

Form	r_x [m]	r_y [m]	r_z [m]	α_x [rad]	α_y [rad]	α_z [rad]
(a)	0.051	0.029	0.008	0.006	0.006	0.047
(b)	0.086	0.089	0.017	0.020	0.018	0.038
(c)	0.144	0.046	0.009	0.005	0.016	0.039

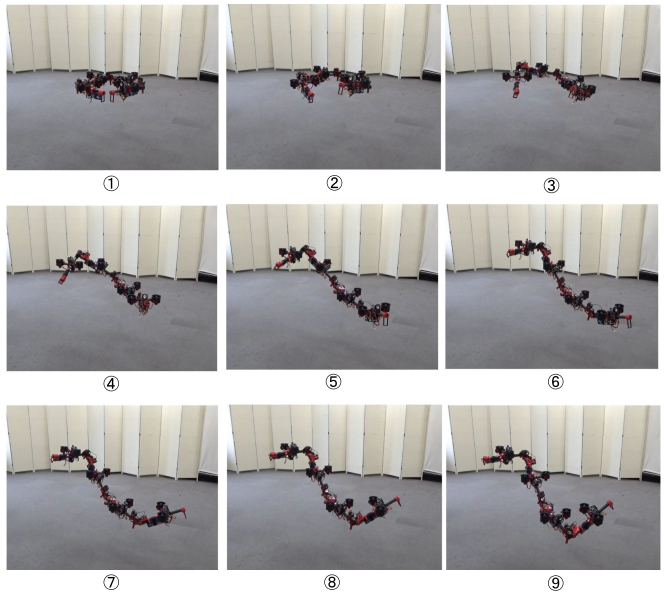

Fig. 7. The snapshot for the aerial transform of quad-type DRAGON.

errors as shown in Table III still demonstrates the high degree of stability of hovering control under these fixed forms.

C. Aerial Transformation

The large-scale aerial transformation is performed with the following start and unique goal forms:

$$\begin{cases} Start: \boldsymbol{q}_d = (0 \quad 1.57 \quad 0 \quad 1.57 \quad 0 \quad 1.57)^{\mathrm{T}}, \\ \qquad\qquad (\Psi_d, \Theta_d, \Phi_d) = (0, 0, 0) \\ Goal: \boldsymbol{q}_d = (-0.6 \quad -1.57 \quad -0.6 \quad 0 \quad 0 \quad 1.57)^{\mathrm{T}}, \\ \qquad\qquad (\Psi_d, \Theta_d, \Phi_d) = (0, -0.3, 0) \end{cases}$$

To satisfy the assumption of regarding the multilinked robot as a single rigid body for flight control, the rotation speed of each joint is set as 0.17 [rad/s]. After transformation, the robot was kept hovering under the goal form. The snapshots and related plots in Figs. 7 and 8 indicate the relatively stable hovering under the transformation.

The RMS tracking errors are r_x: 0.143 [m], r_y: 0.145 [m], r_z :0.016 [m], α_x: 0.019 [rad], α_y: 0.018 [rad], and α_z: 0.060 [rad]. The relatively large tracking error about horizontal motion is also observed because of the saturation of the thrust force while passing some critical intermediate forms.

According to the proposed control method, the range of aerial transformation is limited because the singularity in the thrust force control would still appear when the rank of modified matrix $Q' = \left(Q(3)^{\mathrm{T}} \; Q(4)^{\mathrm{T}} \; Q(5)^{\mathrm{T}}\right)^{\mathrm{T}}$ from (15) is not full. Therefore, the development of the singularity-free control method is a crucial topic for future research. Despite the limited transformation range, the proposed design and control method ex-

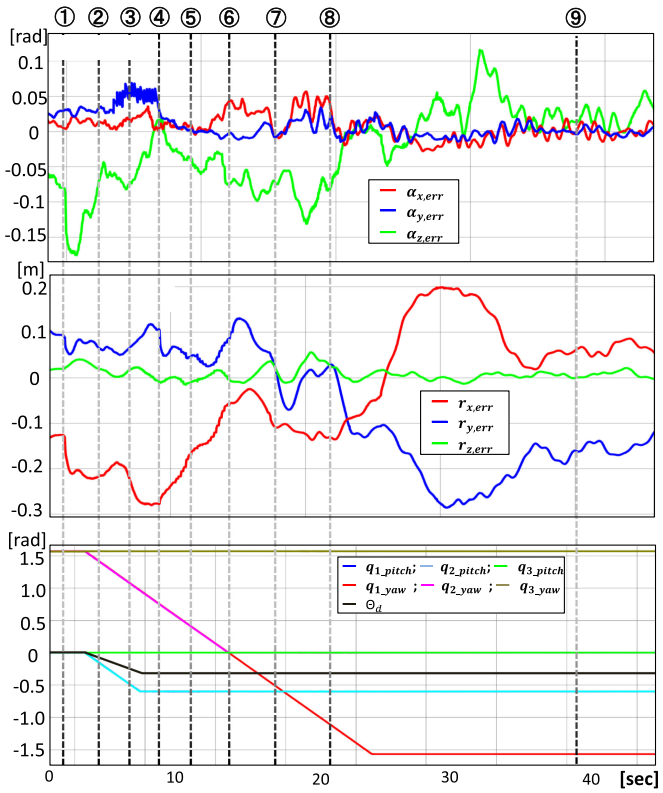

Fig. 8. The tracking errors of six-DoF states associated with the joint angles and desired attitude of baselink (Θ_d). The dotted lines correspond with the representative forms in Fig. 7.

perimentally confirm the feasibility within the relatively large transformation range and also imply that various aerial manipulations can be achieved with the current degree of stability.

VI. Conclusion and Future Work

In this letter, we presented the novel multi-DoF transformable aerial robot DRAGON, which comprises dual-rotor gimbal modules and 2DoF joint modules. The original mechanical design is proposed, followed by an analysis on the variable rotor configuration. The dynamics is derived to achieve the subsequent decoupling flight control, which is separated into the thrust force control and rotor gimbal (vectoring) control. The experimental results confirm the feasibility of hovering under unique fixed forms and large-scale aerial transformation via the prototype comprising four links.

We believe that the robot platform DRAGON can provide more advantages on the high-level maneuvering and aerial manipulation. We will move forward to apply DRAGON in a complex environment and perform tasks such as passing a narrow hole by transformation and grasping and carrying objects by using the ends of the multilinks.

References

[1] C. Papachristos, S. Khattak, and K. Alexis, "Uncertainty-aware receding horizon exploration and mapping using aerial robots," in *Proc. IEEE Int. Conf. Robot. Autom.*, May 2017, pp. 4568–4575.

[2] J. Delmerico, E. Mueggler, J. Nitsch, and D. Scaramuzza, "Active autonomous aerial exploration for ground robot path planning," *IEEE Robot. Autom. Lett.*, vol. 2, no. 2, pp. 664–671, Apr. 2017.

[3] V. Kumar and N. Michael, "Opportunities and challenges with autonomous micro aerial vehicles," *Int. J. Robot. Res.*, vol. 31, no. 11, pp. 1279–1291, 2012.

[4] D. Mellinger, N. Michael, and V. Kumar, "Trajectory generation and control for precise aggressive maneuvers with quadrotors," *Int. J. Robot. Res.*, vol. 31, no. 5, pp. 664–674, 2012.

[5] D. Falanga, E. Mueggler, M. Faessler, and D. Scaramuzza, "Aggressive quadrotor flight through narrow gaps with onboard sensing and computing using active vision," in *Proc. IEEE Int. Conf. Robot. Autom.*, May 2017, pp. 5774–5781.

[6] D. Brescianini and R. D'Andrea, "Design, modeling and control of an omni-directional aerial vehicle," in *Proc. IEEE Int. Conf. Robot. Autom.*, May 2016, pp. 3261–3266.

[7] S. Park, J. Her, J. Kim, and D. Lee, "Design, modeling and control of omni-directional aerial robot," in *Proc. IEEE/RSJ Int. Conf. Intell. Robots Syst.*, Oct. 2016, pp. 1570–1575.

[8] M. Ryll, D. Bicego, and A. Franchi, "Modeling and control of fast-hex: A fully-actuated by synchronized-tilting hexarotor," in *Proc. IEEE/RSJ Int. Conf. Intell. Robots Syst.*, Oct. 2016, pp. 1689–1694.

[9] A. Oosedo, S. Abiko, S. Narasaki, A. Kuno, A. Konno, and M. Uchiyama, "Flight control systems of a quad tilt rotor unmanned aerial vehicle for a large attitude change," in *Proc. IEEE Int. Conf. Robot. Autom.*, May 2015, pp. 2326–2331.

[10] K. Kawasaki, Y. Motegi, M. Zhao, K. Okada, and M. Inaba, "Dual connected bi-copter with new wall trace locomotion feasibility that can fly at arbitrary tilt angle," in *Proc. IEEE/RSJ Int. Conf. Intell. Robots Syst.*, Sep. 2015, pp. 524–531.

[11] V. Lippiello *et al.*, "Hybrid visual servoing with hierarchical task composition for aerial manipulation," *IEEE Robot. Autom. Lett.*, vol. 1, no. 1, pp. 259–266, Jan. 2016.

[12] H. Kim, H. Lee, S. Choi, Y. K. Noh, and H. J. Kim, "Motion planning with movement primitives for cooperative aerial transportation in obstacle environment," in *Proc. IEEE Int. Conf. Robot. Autom.*, May 2017, pp. 2328–2334.

[13] A. E. Jimenez-Cano, J. Martin, G. Heredia, A. Ollero, and R. Cano, "Control of an aerial robot with multi-link arm for assembly tasks," in *Proc. IEEE Int. Conf. Robot. Autom.*, May 2013, pp. 4916–4921.

[14] M. Zhao, K. Kawasaki, K. Okada, and M. Inaba, "Transformable multirotor with two-dimensional multilinks: Modeling, control, and motion planning for aerial transformation," *Adv. Robot.*, vol. 30, no. 13, pp. 825–845, 2016. [Online]. Available: http://dx.doi.org/10.1080/01691864.2016.1181006

[15] C. Bermes, S. Leutenegger, S. Bouabdallah, D. Schafroth, and R. Siegwart, "New design of the steering mechanism for a mini coaxial helicopter," in *Proc. IEEE/RSJ Int. Conf. Intell. Robots Syst.*, Sep. 2008, pp. 1236–1241.

[16] T. Haus, M. Orsag, and S. Bogdan, "Mathematical modelling and control of an unmanned aerial vehicle with moving mass control concept," *J. Intell. Robot. Syst.*, vol. 88, no. 2, pp. 219–246, Dec. 2017.

[17] M. Ryll *et al.*, "6D physical interaction with a fully actuated aerial robot," in *Proc. IEEE Int. Conf. Robot. Autom.*, May 2017, pp. 5190–5195.

[18] "Voliro," Sep. 11, 2017. [Online]. Available: https://www.voliro.ethz.ch/

[19] A. Moutinho, E. Mateos, and F. Cunha, "The tilt-quadrotor: Concept, modeling and identification," in *Proc. IEEE Int. Conf. Auton. Robot Syst. Competitions*, Apr. 2015, pp. 156–161.

[20] M. Muehlebach and R. D'Andrea, "The flying platform—A testbed for ducted fan actuation and control design," *Mechatronics*, vol. 42, no. Suppl. C, pp. 52–68, 2017. [Online]. Available: http://www.sciencedirect.com/science/article/pii/S0957415817300016

[21] T. Lee, "Geometric tracking control of the attitude dynamics of a rigid body on SO(3)," in *Proc. Amer. Control Conf.*, Jun. 2011, pp. 1200–1205.

[22] M. Ramp and E. Papadopoulos, "On modeling and control of a holonomic vectoring tricopter," in *Proc. IEEE/RSJ Int. Conf. Intell. Robots Syst.*, Sep. 2015, pp. 662–668.

[23] P. C. Young and J. C. Willems, "An approach to the linear multivariable servomechanism problem," *Int. J. Control*, vol. 15, no. 5, pp. 961–979, 1972.

[24] T. Anzai *et al.*, "Multilinked multirotor with internal communication system for multiple objects transportation based on form optimization method," in *Proc. IEEE/RSJ Int. Conf. Intell. Robots Syst.*, Sep. 2017, pp. 5977–5984.

[25] S. Lynen, M. W. Achtelik, S. Weiss, M. Chli, and R. Siegwart, "A robust and modular multi-sensor fusion approach applied to MAV navigation," in *Proc. IEEE/RSJ Int. Conf. Intell. Robots Syst.*, Nov. 2013, pp. 3923–3929.